Background-suppressed SRS fingerprint imaging with a fully integrated system using a single optical parametric oscillator

Alberto Lombardini, Pascal Berto, Julien Duboisset, Esben Ravn Andresen, Sandro Heuke, Edlef Büttner, Ingo Rimke, Sébastien Vergnole, Vasyl Shinkar, Philippe de Bettignies, et al.

Research Article | Vol. 28, No. 10 / 11 May 2020 / Optics Express 14490
Optics EXPRESS

Background-suppressed SRS fingerprint imaging with a fully integrated system using a single optical parametric oscillator

ALBERTO LOMBARDINI,[1,2] PASCAL BERTO,[3] JULIEN DUBOISSET,[1] ESBEN RAVN ANDRESEN,[4] SANDRO HEUKE,[1] EDLEF BÜTTNER,[4] INGO RIMKE,[5] SÉBASTIEN VERGNOLE,[6] VASYL SHINKAR,[6] PHILIPPE DE BETTIGNIES,[6] AND HERVÉ RIGNEAULT[1,*]

[1]*Aix Marseille Univ, CNRS, Centrale Marseille, Institut Fresnel, Turing Center for Living Systems, Marseille, France*
[2]*Institut de Biologie de l'École Normale Supérieure (IBENS), École Normale Supérieure, CNRS, INSERM, PSL Research University, Paris 75005, France*
[3]*Sorbonne Paris Cité, Université Paris Descartes, Institut de la vision, CNRS-UMR 7210, Paris, France*
[4]*Univ. Lille, CNRS, UMR 8523 – PhLAM – Physique des Lasers Atomes et Molecules, F-59000 Lille, France*
[5]*APE Angewandte Physik & Elektronik GmbH, Haus N, Plauener Str. 163-165, D-13053 Berlin, Germany*
[6]*HORIBA Scientific 231 rue de Lille F-59650 Villeneuve d'Ascq, France*
[*]*herve.rigneault@fresnel.fr*

Abstract: Stimulated Raman Scattering (SRS) imaging can be hampered by non-resonant parasitic signals that lead to imaging artifacts and eventually overwhelm the Raman signal of interest. Stimulated Raman gain opposite loss detection (SRGOLD) is a three-beam excitation scheme capable of suppressing this nonlinear background while enhancing the resonant Raman signal. We present here a compact electro-optical system for SRGOLD excitation which conveniently exploits the idler beam generated by an optical parametric oscillator (OPO). We demonstrate its successful application for background suppressed SRS imaging in the fingerprint region. This system constitutes a simple and valuable add-on for standard coherent Raman laser sources since it enables flexible excitation and background suppression in SRS imaging.

1. Introduction

Coherent Raman scattering (CRS) microscopy [1] is a class of optical imaging techniques based on the photo-stimulation of molecular vibrations. Similarly to spontaneous Raman scattering, the vibrational response provides a specific chemical signature of samples under investigation. The stimulated nature of CRS processes increases the signal levels by several orders of magnitude if compared to the spontaneous process, which allows for faster imaging rates.

In the typical implementation of CRS microscopy, two laser beams (pump and Stokes) of frequency ω_p and ω_S ($\omega_p > \omega_S$) interact with a sample. If the energy difference between pump and Stokes photons matches the energy of a Raman-active molecular vibration ($\Omega_R = \omega_p - \omega_S$), several light scattering processes take place [2,3]. Coherent anti-Stokes Raman scattering (CARS) [4] and stimulated Raman scattering (SRS) [5,6] are the most commonly used in vibrational imaging. Since the two have similar performance in terms of sensitivity [7], SRS is sometimes preferred over CARS because of the absence of non-resonant four wave mixing (FWM) background and the linearity of the signal with molecular concentration. SRS causes the depletion of the pump beam (SRL) and a gain in the Stokes beam (SRG), with part of the electromagnetic energy transferred to the material as vibrational energy. Since the intensity variation is very small with respect to the total power (typ. $\Delta I/I \approx 10^{-5} - 10^{-6}$), high-frequency modulation schemes are usually employed

#390381 https://doi.org/10.1364/OE.390381
Journal © 2020 Received 14 Feb 2020; revised 17 Apr 2020; accepted 17 Apr 2020; published 28 Apr 2020

Optics EXPRESS

to separate the resonant signal from the constant laser power. In a typical scheme, one beam is amplitude modulated at MHz frequencies while the other one is detected with a photodiode. On top of this initially unmodulated beam, the SRS signal appears as a periodic intensity variation that can be extracted using a lock-in amplifier. The use of MHz modulation frequencies allows for short pixel dwell times and for filtering of the low frequency (<1MHz) laser noise.

Today, CRS microscopy is an established imaging modality, with a wide range of applications in biomedical research [8–10]. The vast majority of applications have focused on the high-energy C-H stretch region (2800-3000 cm^{-1}), where strong signals are detected and valuable information about lipids, nucleic acids and proteins is obtained. Applications of CRS in the so-called fingerprint region (500-1800 cm^{-1}) have been more recently explored [11]. Here, vibrational spectra display a higher degree of heterogeneity, which is important for differentiation of multiple species. However, the intensity of Raman signals in the fingerprint is often lower as compared to the high-wavenumber region and the presence of parasitic signals can overwhelm the resonant response, leading to erroneous interpretation of the images [12].

In fact, while free from the non-resonant FWM signal affecting CARS detection, SRS microscopy has other sources of background. Spurious signals are due to competing pump-probe processes that induce a modulation transfer between the excitation beams and erroneously interpreted as SRS signal. These effects can originate from the resonant or the non-resonant electronic response and include two-color, two-photon absorption (TPA), excited-state absorption (ESA), cross-phase modulation (XPM) and thermal lensing (TL) [12–17]. In TPA, a pump and a Stokes photon are simultaneously absorbed to excite the transition of a molecule on a higher electronic state. ESA occurs when a molecule absorb a photon from one beam and interacts with the second beam. ESA is often studied in pump-probe experiments via time-resolved measurements [18] but it represents a spurious signal in the SRS configuration of detection. TL and XPM are two effects arising from local variations in the refractive index. The first one is due to temperature variations induced by heat dissipation from molecules that underwent absorption. XPM is an instantaneous variation of the refractive index seen by one beam that is induced by the other beam. Although XPM can be prevented with a larger collection numerical aperture, scattering samples such as biological tissues enlarge the k-vectors distribution [12]. All these sources of background make SRS imaging in the fingerprint quite challenging. This is especially true in presence of endogenous fluorophores, in pigmented environments or more generally with any absorbing molecules. Practical examples of impeding nonlinear background include melanin in skin tissues [13], hemoglobin in blood vessels [13,17,19], chlorophyll and carotenoids absorption in plants [16,20] but also various sources of nonlinear background in mineralogical samples [15,21].

For the above reasons, most works addressing SRS imaging in the fingerprint region have developed an excitation scheme that deals with non-resonant background. For instance, polarization modulation of the Stokes beam has been shown to suppress the XPM-generated background [14]. In general, the acquisition of SRS images at different spectral points allows the discrimination of the resonant contribution in the signal [15]. In frequency-modulation SRS (FM-SRS), two images (on and off the targeted resonance) are simultaneously acquired and any spectrally flat contribution to the signal is suppressed. This type of excitation has been implemented with picosecond sources by either using two optical parametric oscillators (OPOs) [10,22] or by adding a fiber amplifier to the OPO [17]. Femtosecond sources have also been used: by properly shaping the excitation pulses one can retain sufficient spectral resolution and exploit the broad frequency spectrum for fast wavelength tuning. Frequency modulation has been implemented using an angle-to-wavelength AOM based converter [13] or in combination with spectral focusing [23–25]. While successfully operating background-suppressed SRS imaging, these excitation schemes require significant engineering effort (pulse shaping) or cost (due to additional laser sources).

Optics EXPRESS

A different excitation scheme based on the simultaneous detection of the stimulated Raman gain and loss (SRGOLD) has been proposed to suppress non-resonant background and enhance the resonant signal [12]. SRGOLD excitation requires three beams at different frequency: $\omega_0 - \Omega$, ω_0 and $\omega_0 + \Omega$. One main advantage, it can be implemented with the same OPO source commonly used in SRS and CARS microscopy, by exploiting the usually neglected idler beam. An additional amplitude modulator represents the sole major modification for SRGOLD over a standard SRS setup.

In this article we present a compact module for SRGOLD excitation and its application to background-suppressed CRS imaging of different samples. In a compact module, all the elements required to control the excitation beams delivered by a commercial OPO are assembled. Two EOMs modulate the signal and idler beam with phase-locked, 180 degrees shifted waveforms. A user-friendly software allows control of the transmitted power and the temporal delay of each beam. After presenting the system, we will discuss the applications of the SRGOLD system for nonlinear imaging of different samples, from crystalline calcite to the walls of red onion cells. We show how backgrounds of different origins are suppressed while resonant signals are enhanced. We finally compare SRGOLD with other background suppression methods.

2. Implementation of an SRGOLD microscope

2.1. SRGOLD excitation

SRGOLD excitation exploits both the common pump laser-OPO architecture used in CRS microscopy and the phase-sensitive nature of lock-in detection. The first one assures an equal frequency difference between the fixed frequency (ω_0) beam and the two tunable OPO beams, the signal ($\omega_0 + \Omega$) and the idler ($\omega_0 - \Omega$). When this frequency difference matches the energy of a Raman resonance ($\Omega = \Omega_R$), the ω_0 beam experiences an intensity gain due to the signal beam (SRG) and a loss due to the idler beam (SRL). However, if the idler modulation is π-shifted with respect to the signal beam modulation (and the lock-in reference waveform), the Raman loss in the ω_0 beam is seen as a gain through the lock-in amplifier. The resonant SRG and SRL signals then sum up in the total SRGOLD signal, instead of canceling each other out.

On the other hand, the intensity modulation due to parasite signals has the same net effect (loss or gain) on the ω_0 beam, independently of which other beam is participating in the process. For instance, photon absorption due to TPA and ESA always results in a loss. Thus, parasite signals of this type will cancel each other out in the SRGOLD scheme, because of the opposite phase modulation. This picture equally holds in the case of XPM and thermal lensing. A consideration on the spectral dependence of each process is now necessary. While XPM is spectrally flat, the intensity of TPA and ESA vary with the excitation wavelengths. In order to suppress these parasite signals in SRGOLD mode, one should adjust the relative powers of the signal and idler beam, to make the magnitude of the signal generated by the two beams equal. In most cases, the background due to TPA and ESA is lower when using longer excitation wavelengths [26] (therefore in the SRL case).

2.2. Integrated module for SRGOLD excitation

We have developed a compact and integrated system for SRGOLD excitation, which can be coupled to any OPO source pumped by a frequency doubled Ytterbium [27] or Neodymium laser (1031 nm, 1040 nm or 1064 nm). This system is designed for the control of spatially overlapped, collimated beams that are split each in one of the three paths, according to their wavelength (signal < 1000 nm, idler >1100 nm and ω_0 beam). The SRGOLD module (Fig. 1(b)) provides all the elements for spatial and temporal control of the pulses, power adjustment and phase-locked high-frequency modulation. Most elements are software-controlled through a user-friendly GUI

Optics EXPRESS

(except for spatial alignment which is mechanically operated). The SRGOLD module has been designed to be ideally added after the CRS laser system picoEmerald manufactured by APE.

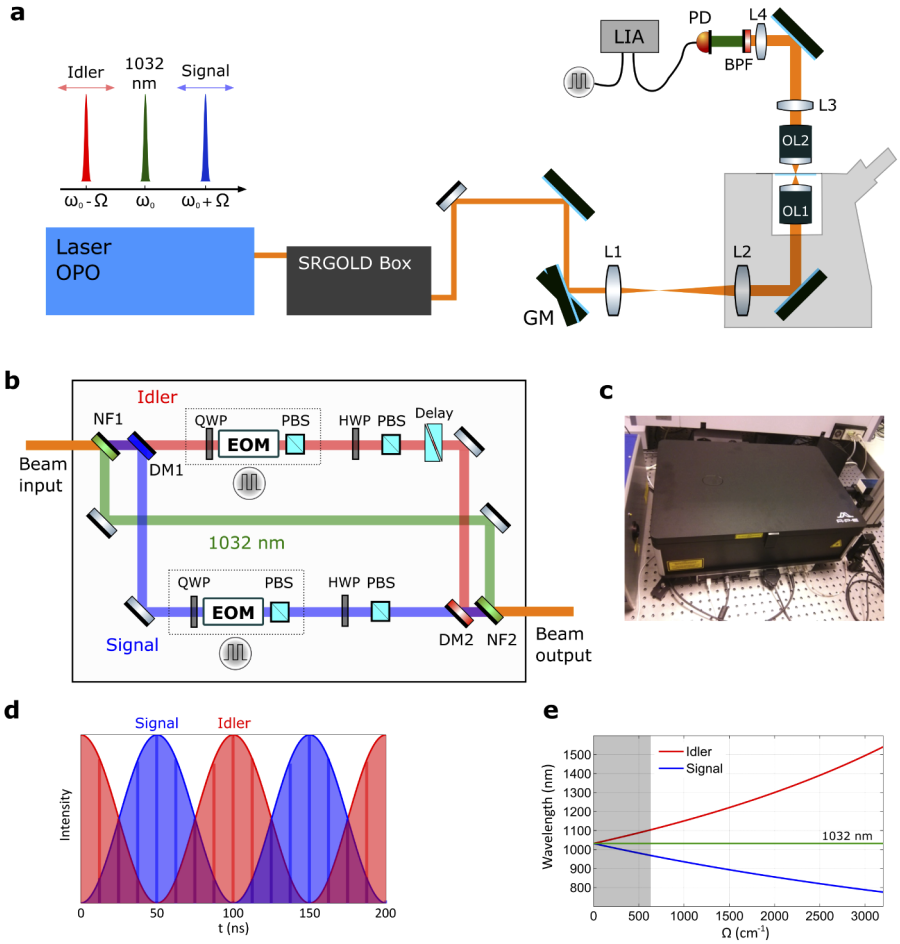

Fig. 1. (a) Nonlinear microscope for SRS and SRGOLD imaging. GM: Galvanometric mirrors; L1-L4: achromatic lenses; OL1,OL2: Objective lenses; BP: Bandpass filter; PD: Photodiode; LIA: Lock-in amplifier. (b) Schematic representation of the SRGOLD module. DM1,DM2: Dichroic mirrors. NF1, NF2: Notch filters. QWP: Quarter-wave plate; EOM: Electro-optical modulator, PBS: Polarizing beamsplitter, HWP: Half-wave plate. Note that the delay of the fixed wavelength beam is controlled directly with OPO built-in delay line (APE-PicoEmerald). (c) Close-up view of the SRGOLD module (80cm x 50cm x 20cm). (d) Representation of the 10 MHz modulation waveforms over two cycles for the signal and idler beam. (e) Excitation beam wavelength as a function of the targeted wavenumber. The area in grey is the excluded wavenumber region which cannot be accessed with the SRGOLD module (limitation imposed by the filters).

The beams are split and recombined by a series of dichroic mirrors: two custom laser line mirrors (highly reflecting at 1030 nm) splits and recombine the ω_0 beam (NF1 and NF2 in Fig. 1(b)) while a custom longpass dichroic mirror (T>90% between 1150-2300 nm) separates the signal from the idler and a shortpass dichroic mirror (DMSP 1000, Thorlabs) recombines the beams (DM1 and DM2 Fig. 1(b), respectively).

Optics EXPRESS

Intensity modulation of the signal and idler beams is performed by two electro-optical modulators (EOMs, Thorlabs) operated in a master-slave configuration. Each EOM is preceded by a quarter-wave plate ($\lambda/4$) and followed by a polarizing beam-splitter, which turns the polarization rotation into a sinusoidal intensity modulation. The EOM are driven by a 10 MHz waveform, derived from the 80 MHz signal of the laser through a frequency divider. The EOMs are part of a resonant 10 MHz circuit that provides a high-voltage sinusoidal waveform with relatively low power consumption compared to non-resonant driving. By properly adjusting the $\lambda/4$ the idler and signal beam can achieve an optimal π – shifted sinusoidal modulation (Fig. 1(d)). Power control of the idler and signal beams is performed independently with a half-wave plate coupled to a polarizer. A double wedge provides mechanical control of the optical delay in the idler's path over a 15 ps window. The temporal delay of the ω_0 beam is adjusted with a mechanical delay line in the laser system (APE, PicoEmerald). The signal and idler wavelengths can be tuned automatically from the OPO to address the 600 cm^{-1}-3200 cm^{-1} wave-number range ((Fig. 1(e)).

2.3. Nonlinear microscope with the integrated module for SRGOLD excitation

SRGOLD (and SRS) detection can be implemented on a standard nonlinear microscope (Fig. 1(a)), provided that a suitable laser source is available and by adding a few elements for (a) the modulation of one excitation beam and (b) the frequency resolved lock-in detection. In our setup the laser source is provided by a picoEmerald system (APE GmbH, Germany). It consists of a solid state OPO pumped by a frequency doubled Ytterbium (Yb) fiber laser (Aeropulse, NKT Photonics). The Yb laser provides one excitation beam itself, at the fixed wavelength of 1031 nm, with pulses having 2 ps duration and 80 MHz repetition rate. The other two excitation beams are generated by the OPO and can be tuned between 700 nm and 990 nm (signal) and 1100 nm and 1900 (idler). The use of 2 ps pulses is a good tradeoff between short pulse duration and spectral resolution (10 cm^{-1}).

The optical path is depicted in Fig. 1(a): three spatially overlapped beam delivered by the laser are coupled in the SRGOLD system. After manipulation and recombination in the module (as described in the previous section), the pulses are directed to the galvanometric mirrors (6220H, Cambridge Technology) whose intermediate plane is conjugated by a telescope to the objective's back aperture. The scan lens (100 mm, AC254-100-B, Thorlabs) and tube lens (200 mm, AC254-200-B, Thorlabs) provide a total magnification of 2. A mirror in the microscope (Nikon Eclipse Ti) redirects the beams in the vertical direction, where the excitation objective (20x, 0.45 NA, Olympus or 20x, 0.75 NA Nikon) focuses them into the sample. A second objective (20x, 0.7 NA, Nikon) collects and collimates the beams and another telescope (200 mm and 75 mm focal lengths respectively) conjugates the back-aperture with a photodiode's clear aperture. Before the photodiode, two premium bandpass filters (FLH1030-10, Thorlabs) totally block any detectable signal and idler residue (optical density larger than 5 between 800 nm and 1010 nm, and 1050 nm and 1200 nm). The ω_0 beam is then detected by a silicon-based photodiode connected to a lock-in amplifier (APE GmbH), seeded with the 10 MHz waveform from the modulator. The lock-in output signal is proportional to the modulation depth in the ω_0 beam.

3. Results

In order to validate the capability of the SRGOLD system to suppress artefacts and enhance the Raman signals we image different samples, such as polymer (beads), crystalline (calcite) and biological samples (plant cells). To better appreciate the difference between two-beam excitation schemes (SRL and SRG) and the SRGOLD one, we present images obtained with the three contrasts. All images are acquired using a lock-in time constant of 20 μs and a pixel-dwell time between 40 and 400 μs (depending on the image). We use a color bar that displays positive

Optics EXPRESS

values of the SRS signal in red-yellow colors, while negative values are displayed in blue. Zero signal are represented in black.

3.1. Resonant signals and artifacts in SRS and SRGOLD imaging

The images of Fig. 2 present different samples, where either a Raman resonance or spurious signals are detected. The PMMA beads (6 μm diameter) of Fig. 2(b) are imaged at one of their Raman resonances (812 cm^{-1}) and constitute an example of image with pure Raman signal. In the SRL modality (idler, ω_0), the Raman loss generates a positive signal, because of the opposite phase modulation. In SRG modality (signal, ω_0), the signal beam is modulated in phase and the lock-in output is also positive. The SRGOLD image contains the positive contribution from both SRG and SRL processes, which are added up to provide a x2 signal enhancement. Here, we used excitation powers of 12 mW (idler), 8 mW (signal) and 40 mW (ω_0). The pixel dwell time was fixed to 200 μs.

One of the signatures of non-Raman signals is the opposite sign in SRG and SRL modalities (in the present scheme where SRG and SRL are π phase shifted). The signal detected in Fig. 2(c) (red onion cell) and Fig. 2(d) (PMMA) is positive in the SRL channel and negative in the SRG one. This means that the ω_0 beam experiences a loss both with the signal beam and with the idler beam, which is a different outcome than a stimulated Raman process. The origin of these spurious signals can be different. The signal generated within the pigment-rich red onion cells in Fig. 2(c) is most likely due to a two-color TPA process. By properly tuning the excitation powers (on the sample: P_{idler}=14 mW,P_{signal}=18 mW,P_{ω_0}=60 mW), the TPA signal can be compensated in the SRGOLD mode. As we will see in Sec. 3.3, the three-beam excitation scheme allows much better visualization of cell walls, by both suppressing the background and enhancing the Raman signal.

The PMMA matrix of Fig. 2(d) was imaged off-resonance (1000 cm^{-1}) with a diaphragm placed in front of the photodiode. By slightly clipping the beam, we reproduce the situation occurring when the collection NA is smaller than or equal to the excitation NA. In such a situation, XPM changes the refractive index of the medium and in turn affects the angular spectrum of the detected beam. This ultimately results in a modulation transfer and thus a parasitic signal detected with the lock-in. XPM is spectrally flat [13] and can be cancelled out using the SRGOLD excitation scheme (the small negative offset in the image is due to the lock-in settings during acquisition). The excitation powers at the sample were the following 20 mW (idler), 16 mW (signal) and 50 mW (ω_0). In our setup we used a relatively low excitation NA (0.45) which simplified the use of a higher collection NA (0.7), artificially introducing this XPM artifact demonstrates its efficient cancellation in the SRGOLD modality. However, XPM suppression might become important when aiming for high spatial resolution (therefore using a high NA objective) or imaging in scattering samples, where the beam NA is enlarged [12].

3.2. Calcite crystals

Oyster shells are mainly composed of crystalline calcite ($CaCO_3$) and present a strong Raman resonance at 1087 cm^{-1} [29]. Thus, coherent Raman techniques are ideal for fast imaging of these structures. Nevertheless, a nonlinear background is generated in these samples [15] which makes the signal interpretation difficult. While the origin of this background is not fully understood, the observation of a signal decay with time, some sort of photobleaching (images not shown), suggests that electronic excitation processes might be involved [30].

Figure 3(c) shows that a signal is detected in SRL mode when the excitation is set off-resonance (at 1130 cm^{-1}). Here, we clearly demonstrate the non-Raman origin of this signal as the SRG channel exhibits a negative sign. Although not totally suppressed, the background magnitude is importantly reduced in the SRGOLD image. Images acquired very close to the Raman resonance (1080 cm^{-1}) have a contribution to the signal that is both resonant and non-resonant (Fig. 3(c),

Optics EXPRESS

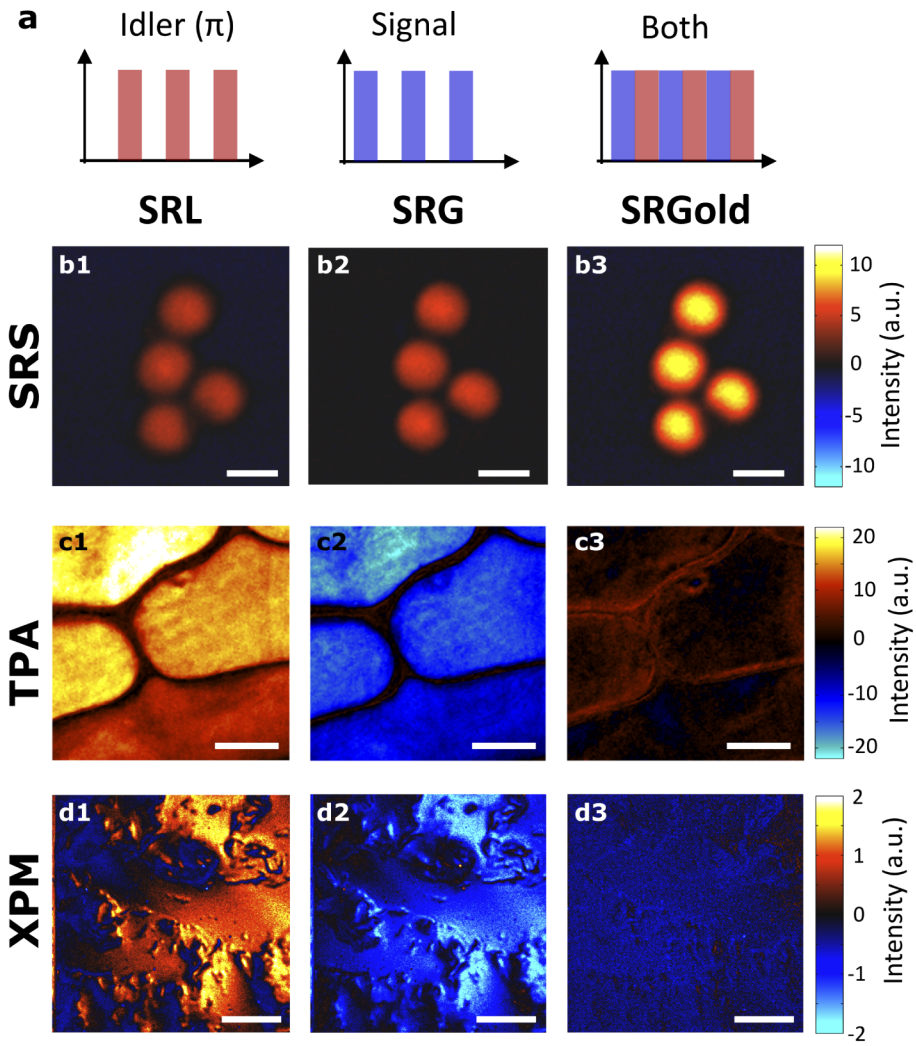

Fig. 2. Lock-in detection of resonant Raman signals and backgrounds. (a) Beam modulation in the different excitation schemes: in the SRL modality, the idler is amplitude modulated with a π phase shift with respect to the lock-in waveform. Losses experienced by the ω_0 beam are seen as positive signal. In the SRG modality, the signal beam is amplitude modulated in phase with the lock-in waveform. In SRGOLD, both the SRL and SRG contributions are detected. (b1-b3) 5 μm PMMA beads imaged at the Raman resonance 812 cm^{-1}; scale bars: 5 μm; . (c1-c3) Red onion cells imaged at 1000 cm^{-1}. A strong non-Raman contribution is generated inside the cells, which is attributed to two-color two-photon absorption (TPA) by the pigments in the plant cells (anthocyanins); scale bars: 40 μm. (d1-d3) Images of a PMMA matrix at the non-resonant frequency of 890 cm^{-1}. A non-resonant signal due to cross-phase modulation (XPM) is detected in two-beam SRS when the detected beam is clipped on the detection path; scale bars: 40 μm. Pixel dwell time 200 μs on all images

Optics EXPRESS

top row). Especially in the case of SRG. The SRGOLD image (third column) provides the best contrast (resonant over non-resonant) thanks to the off-resonance signal reduction. The absolute intensity of the non-resonant signal in calcite crystals is very different in the SRG and SRL channels, when using similar powers. The reason is to be sought in the wavelength-dependency of the process generating the signal, most likely a non-linear absorption in this case. In order to suppress artifacts of this type, the SRGOLD scheme requires adjustment of the idler and signal beam intensity. The relative signal to idler power will depend on the absorption spectrum of the molecular species generating the background. The excitation powers used for images of Fig. 3 are : 12 mW (idler), 2.5 mW (signal) and 40 mW (ω_0), measured at the sample plane.

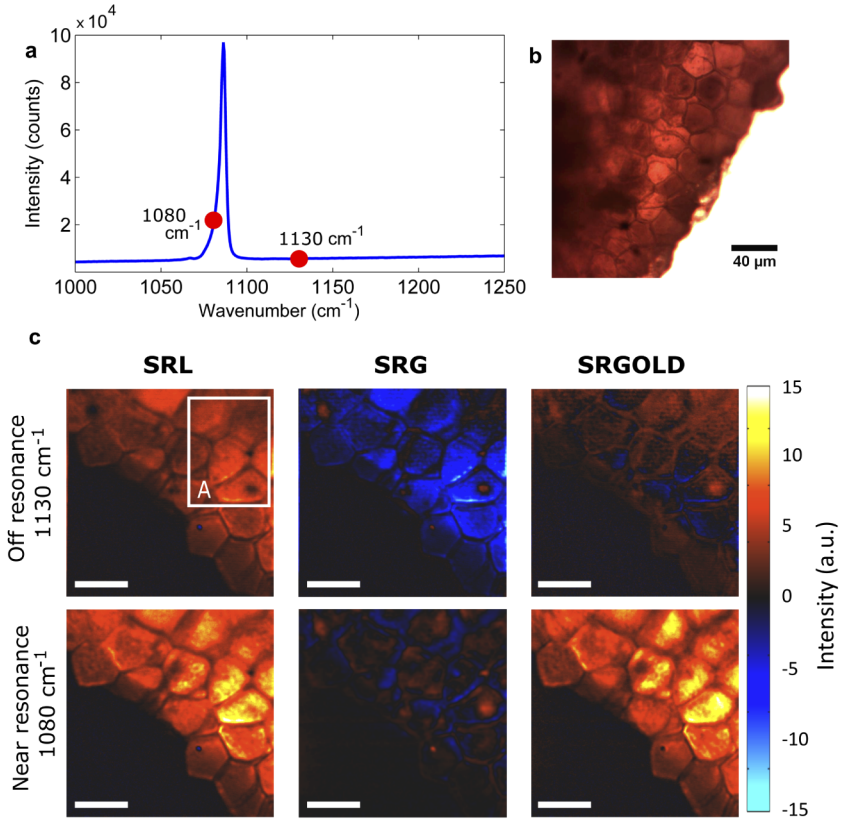

Fig. 3. SRS imaging of calcite crystals from an oyster shell. (a) Spontaneous Raman spectrum of crystalline calcite ($CaCO_3$)) obtained from [28] and (b) white light image of the sample. (c) SRS images acquired at two different spectral positions: off-resonance (1130 cm^{-1}, top row) and near the resonance (1080 cm^{-1}, bottom row). For each spectral position the images acquired in SRG, SRL and SRGOLD modality (from left to right) are displayed. The non-resonant background found in standard two-beams SRS (SRL and SRG) is partially suppressed in the SRGOLD modality, where the resonant signal is also enhanced. The area enclosed by the white box in the non-resonant SRL image was used to estimate the background suppression. A low-pass filter was applied on the images to remove a periodic electronic noise artefact. Scale bars in (c) 20 μm.

A quantification of the background reduction with SRGOLD can be obtained through the signal to background (SBR) ratio. In our resonance/out of resonance images the signal and

Optics EXPRESS

background are computed as:

$$SBR = Signal/Background = \left|\frac{<I_r> - <I_{nr}>}{<I_{nr}>}\right|$$

where $<I_{nr}>$ is the average value in the out of resonance image (1130 cm^{-1}) and $<I_r>$ is the average value of the image at resonance (1080 cm^{-1}). SRGOLD achieves a 6-fold increase in SBR as compared to SRL excitation (SBR_{SRGOLD} = 4.5, SBR_{SRL} = 0.7), thanks to a suppression of the non-Raman background (B_{SRGOLD} = 1.3 a.u. and B_{SRL} = 4 a.u.) and an increase of the resonant signal due to the contribution of the SRG process ($Signal_{SRGOLD}$ = 5.8 a.u., $Signal_{SRL}$ = 2.9 a.u.).

3.3. SRGOLD imaging in a pigmented environment: red onion cells

SRS imaging in plants is known to be disturbed by the presence of pigments that generates strong parasitic signals [16]. We apply the SRGOLD excitation scheme to two different pigmented vegetables: red onion cells (pigments: anthocyanins) and carrots (carotenoids). Onion cells are often used as a reference sample to study the plant cell's structure. A single cellular layer can easily be obtained: it is composed of highly-ordered, elongated cells (white light image in Fig. 4(b)). The red color of the cells is due to natural pigments called anthocyanins ([31]). SRS imaging on this sample gives rise to a strong parasitic signal within cell bodies (negative sign in the SRG channel, Fig. 4(a)). This signal has a negligible spectral variation over 200 cm^{-1} and we attribute its origin to a two-color TPA process from the anthocyanins. The parasitic signal is similarly found in the SRL channel (idler-ω_0). By finely tuning the excitation powers (at the sample: signal 18 mW; idler 12 mW; ω_0 68 mW) one can cancel out the parasitic signal within cell bodies (SRGOLD images in Fig. 4(c)).

Besides background suppression, our interest lies in whether we can visualize cell structures through their Raman resonance. Plant cell walls have been visualized by means of spontaneous Raman imaging in some recent works [32] [33]. In these studies, the Raman resonance of cellulose, peaking around 1090 cm^{-1} [34], was exploited; cellulose is the main constituent of these cells' walls. This same Raman resonance can be exploited in SRS, provided that the non-resonant background is suppressed. We demonstrate this by subtraction of resonant and off-resonant image (Fig. 4(d)), where the latter is acquired at 1000 cm^{-1}. This images mimic frequency-modulation schemes and demonstrate that the 1090 cm^{-1} resonance can be used to visualize the cellulose in cell walls. With SRGOLD we can also extract the resonant Raman contribution to the signal, which is non-zero in the cell walls for both wavenumbers, with a significant increase at 1090 cm^{-1}.

3.4. SRS in presence of a wavelentgh un-symmetric background

Carotenoids are pigments that can be found in orange vegetables, such as carrots, orange-fleshed sweet potatoes and mangoes. Brackmann and coworkers [35] combined CARS (at the 1520 cm^{-1} Raman resonance) and second harmonic generation (SHG) imaging to study β-carotene and starch granules distribution in different plant cells. SRS imaging of such molecules is affected by the background originating from nonlinear absorption. The intensity of such background depends on the excitation wavelengths. Off resonance (Ω =1560 cm^{-1}, top row Fig. 5) the SRG and SRL channels display very different behavior. While practically no signal is found in the SRL mode, an intense parasitic signal is generated in SRG. At resonance (Ω =1520 cm^{-1}) a positive (Raman) signal is generated in both excitation modes. In the SRL mode the image contains only the Raman signal, given the absence of a non-resonant background. In the SRG mode, the image results from superposition of resonant and non-resonant contributions. The subtraction of the non-resonant signal from the resonant image (frequency modulation-like operation, in the third row of Fig. 5) allows to retrieve, in the SRG channel, the pure Raman contribution. Such an image (FM-SRG) correlates remarkably well with the resonant SRL image, for both (a) the

Optics EXPRESS

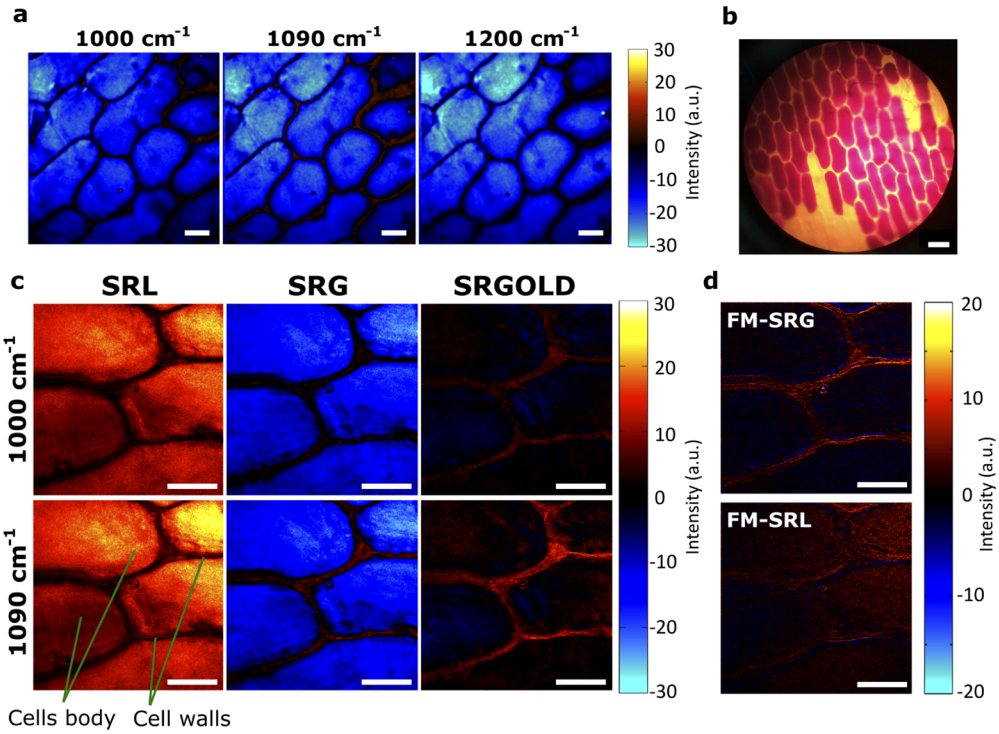

Fig. 4. SRS imaging of red onion cells. (a) SRG images acquired at different spectral positions. A spectrally independent, negative (therefore non-Raman) signal is detected within the cell bodies. We attribute this signal to two-color TPA by the pigments (anthocyanines) within the cells, responsible for the red color seen in the white light image in (b). (c) From left to right: SRL, SRG and SRGOLD images acquired at two different spectral positions: 1000 cm^{-1} (top row) and 1090 cm^{-1} (bottom row), the latter one corresponding to a resonance in the spectrum of cellulose. SRGOLD excitation suppresses the parasitic background signal generated in the cell body, while enhancing the Raman resonant signal generated at the cell walls. The white boxes (B and S) in the SRL image at 1000 cm^{-1} define the areas which were used for SBR quantification. (d) The cell walls can be equally visualized by subtraction of the 1090 cm^{-1} (resonance) and 1000 cm^{-1} (off-resonance) images, reproducing frequency-modulation schemes. Scale bars: (a) 50 μm; (b) 100 μm; (c) and (d) 50 μm. Pixel dwell time : 0.4 ms

Optics EXPRESS

potato and (b) the carrot roots. This is an example where the SRGOLD modality fails to cancel the non-resonant contribution due to its very different contribution in the SRL and SRG images. However the SRGOLD module allows discrimation of the Raman signal from the artefacts and can still provide a SRL background free image.

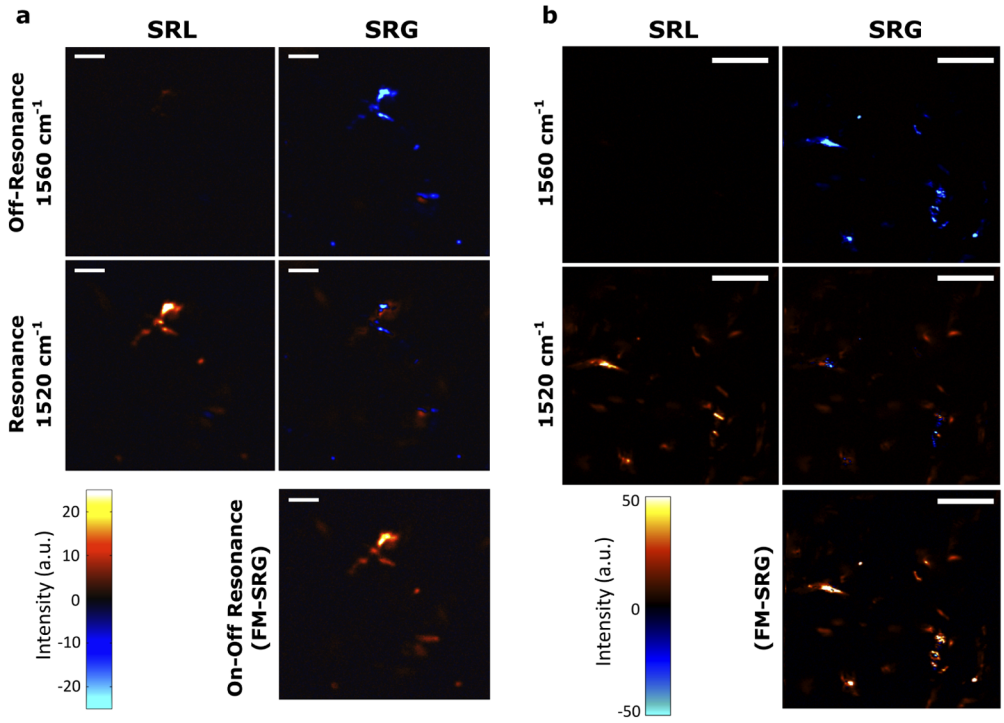

Fig. 5. SRS imaging of carotenoids in: (a) an orange-fleshed sweet potato root; (b) a carrot root. Carotenoids have a Raman resonance at 1520 cm^{-1}, while 1560 cm^{-1} can be taken as the non-resonant Ref. [35]. A strong off-resonance background is generated in the SRG mode, while absent in the SRL channel. The resonant SRL image have a good correlation to the background-subtracted SRG. Excitation powers (at the sample): signal 7 mW; idler 20 mW; ω_0 25 mW. Scale bars: (a) 10 μm; (b) 40 μm; pixel dwell time: 0.2 ms

4. Discussion and conclusion

The results of the last sections are a good starting point for a discussion of SRGOLD excitation applications. Artifact suppression with this three-beam scheme is based on the possibility to balance the weight of parasitic signals in the two channels (SRG and SRL). This is possible when the artifact is generated in both channels and the excitation powers can be adjusted to achieve satisfactory suppression. The SRGOLD signal is also enhanced by adding the Raman contributions of SRL with SRG. Unfortunately, when multiple artifact sources are present, such as multiple pigment types with different absorption spectra, SRGOLD cannot simultaneously suppress them. This is due to the relative idler and signal beam powers needed for suppression being different for each artifact. There are also situations where artifacts arise in one excitation channel only. This is the case of carotenoids SRS imaging around 1500 cm^{-1}: a strong parasite signal is generated in the SRG mode while it is absent in the SRL channel. In such a sample, SRGOLD cannot suppress the artifacts generated with the signal and ω_0 beams. However, the SRL image is a background-free image itself, since the long idler and ω_0 excitation

Optics EXPRESS

wavelengths avoid nonlinear absorption (and employs lower laser power) thus reducing the risk of photodamage and bleaching associated with it [30]. The SRGOLD module allows SRS imaging with excitation wavelengths longer than those typically employed. This might be beneficial for deeper penetration in biological tissues has been recently prospected [36]. When implemented in the proposed scheme (OPO picoEmerald with the SRGOLD box), hyperspectral SRGOLD can be performed over a limited vibrational frequency range (few hundreds of cm^{-1}) as soon as chromatic aberrations are not detrimental to the SRGOLD three beams overlap along the z axis. Compared to FM-SRS using spectral focusing [13,23–25] SRGOLD is adapted to ps sources and can be implemented over a large vibrational frequency range with no or little optical adjustment; indeed the dispersion management in spectral focusing is very wavelength dependent [37].

We have presented an electro-optomechanical system that was designed to provide flexible excitation in SRS and allow a user-friendly implementation of SRGOLD excitation. The system was characterized and proved to perform background-free SRS imaging in presence of pigments or XPM contribution (present in scattering media). This integrated system can be coupled to any OPO source pumped by a frequency doubled 1031 nm or 1064 nm laser. It is cost-effective, because it exploits a beam, the idler, which is intrinsically generated by laser systems very often employed in SRS microscopy. Moreover, it is relatively simple to implement on a microscope setup, since it does not require pulse shaping techniques often employed in background suppression schemes. SRGOLD is very effective when cancelling out the parasitic signals generated by one single molecular species, as demonstrated on different samples of geological and biological interest.

Funding

Centre National de la Recherche Scientifique; Aix-Marseille Université (A-M-AAP-ID-17-13-1702228-15.22-RIGNEAULT); A*Midex (ANR-11- IDEX-0001-02); Cancéropôle Provence-Alpes Côte d'Azur, National Cancer Institute, Région Sud, Agence Nationale de la Recherche ANR–10-INSB-04-01, ANR-11-INSB-0006, ANR-16-CONV-0001); Institut National de la Santé et de la Recherche Médicale (PC201508, 18CP128-00); National Institute of Health(R21EB025389, R21MH117786).

Disclosures

The content is solely the responsibility of the authors and does not necessarily represent the official views of the US National Institutes of Health.

References

1. J.-X. Cheng and X. S. Xie, *Coherent Raman scattering microscopy* (CRC press, 2016).
2. R. W. Boyd, *Nonlinear optics* (Elsevier, 2003).
3. H. Rigneault and P. Berto, "Tutorial: Coherent raman light matter interaction processes," APL Photonics **3**(9), 091101 (2018).
4. A. Zumbusch, G. R. Holtom, and X. S. Xie, "Three-dimensional vibrational imaging by coherent anti-stokes raman scattering," Phys. Rev. Lett. **82**(20), 4142–4145 (1999).
5. C. W. Freudiger, W. Min, B. G. Saar, S. Lu, G. R. Holtom, C. He, J. C. Tsai, J. X. Kang, and X. S. Xie, "Label-free biomedical imaging with high sensitivity by stimulated raman scattering microscopy," Science **322**(5909), 1857–1861 (2008).
6. P. Nandakumar, A. Kovalev, and A. Volkmer, "Vibrational imaging based on stimulated raman scattering microscopy," New J. Phys. **11**(3), 033026 (2009).
7. Y. Ozeki, F. Dake, S. Kajiyama, K. Fukui, and K. Itoh, "Analysis and experimental assessment of the sensitivity of stimulated raman scattering microscopy," Opt. Express **17**(5), 3651–3658 (2009).
8. C. H. Camp Jr and M. T. Cicerone, "Chemically sensitive bioimaging with coherent raman scattering," Nat. Photonics **9**(5), 295–305 (2015).
9. I. W. Schie, C. Krafft, and J. Popp, "Applications of coherent raman scattering microscopies to clinical and biological studies," Analyst **140**(12), 3897–3909 (2015).

Optics EXPRESS

10. B. Sarri, R. Canonge, X. Audier, E. Simon, J. Wojak, F. Caillol, C. Cador, D. Marguet, F. Poizat, M. Giovannini, and H. Rigneault, "Fast stimulated raman and second harmonic generation imaging for intraoperative gastro-intestinal cancer detection," Sci. Rep. **9**(1), 10052 (2019).
11. C. H. Camp Jr, Y. J. Lee, J. M. Heddleston, C. M. Hartshorn, A. R. H. Walker, J. N. Rich, J. D. Lathia, and M. T. Cicerone, "High-speed coherent raman fingerprint imaging of biological tissues," Nat. Photonics **8**(8), 627–634 (2014).
12. P. Berto, E. R. Andresen, and H. Rigneault, "Background-free stimulated raman spectroscopy and microscopy," Phys. Rev. Lett. **112**(5), 053905 (2014).
13. D. Zhang, M. N. Slipchenko, D. E. Leaird, A. M. Weiner, and J.-X. Cheng, "Spectrally modulated stimulated raman scattering imaging with an angle-to-wavelength pulse shaper," Opt. Express **21**(11), 13864–13874 (2013).
14. M. Andreana, M.-A. Houle, D. J. Moffatt, A. Ridsdale, E. Buettner, F. Légaré, and A. Stolow, "Amplitude and polarization modulated hyperspectral stimulated raman scattering microscopy," Opt. Express **23**(22), 28119–28131 (2015).
15. M.-A. Houle, R. C. Burruss, A. Ridsdale, D. J. Moffatt, F. Légaré, and A. Stolow, "Rapid 3d chemical-specific imaging of minerals using stimulated raman scattering microscopy," J. Raman Spectrosc. **48**(5), 726–735 (2017).
16. J. C. Mansfield, G. R. Littlejohn, M. P. Seymour, R. J. Lind, S. Perfect, and J. Moger, "Label-free chemically specific imaging in planta with stimulated raman scattering microscopy," Anal. Chem. **85**(10), 5055–5063 (2013).
17. W. Yang, A. Li, Y. Suo, F.-K. Lu, and X. S. Xie, "Simultaneous two-color stimulated raman scattering microscopy by adding a fiber amplifier to a 2 ps opo-based srs microscope," Opt. Lett. **42**(3), 523–526 (2017).
18. X. Audier, N. Balla, and H. Rigneault, "Pump-probe micro-spectroscopy by means of an ultra-fast acousto-optics delay line," Opt. Lett. **42**(2), 294–297 (2017).
19. D. Fu, T. Ye, T. E. Matthews, B. J. Chen, G. Yurtserver, and W. S. Warren, "High-resolution in vivo imaging of blood vessels without labeling," Opt. Lett. **32**(18), 2641–2643 (2007).
20. D. Fu, F.-K. Lu, X. Zhang, C. Freudiger, D. R. Pernik, G. Holtom, and X. S. Xie, "Quantitative chemical imaging with multiplex stimulated raman scattering microscopy," J. Am. Chem. Soc. **134**(8), 3623–3626 (2012).
21. M.-C. Kao, A. F. Pegoraro, D. M. Kingston, A. Stolow, W.-C. Kuo, P. H. Mercier, A. Gogoi, F.-J. Kao, and A. Ridsdale, "Direct mineralogical imaging of economic ore and rock samples with multi-modal nonlinear optical microscopy," Sci. Rep. **8**(1), 16917 (2018).
22. S. Heuke, B. Sarri, X. Audier, and H. Rigneault, "Simultaneous dual-channel stimulated raman scattering microscopy demultiplexed at distinct modulation frequencies," Opt. Lett. **43**(15), 3582–3585 (2018).
23. D. Fu, W. Yang, and X. S. Xie, "Label-free imaging of neurotransmitter acetylcholine at neuromuscular junctions with stimulated raman scattering," J. Am. Chem. Soc. **139**(2), 583–586 (2017).
24. R. He, Y. Xu, L. Zhang, S. Ma, X. Wang, D. Ye, and M. Ji, "Dual-phase stimulated raman scattering microscopy for real-time two-color imaging," Optica **4**(1), 44–47 (2017).
25. T. Ito, Y. Obara, and K. Misawa, "Invited article: Spectral focusing with asymmetric pulses for high-contrast pump–probe stimulated raman scattering microscopy," APL Photonics **3**(9), 092405 (2018).
26. D. Zhang, M. N. Slipchenko, and J.-X. Cheng, "Highly sensitive vibrational imaging by femtosecond pulse stimulated raman loss," J. Phys. Chem. Lett. **2**(11), 1248–1253 (2011).
27. I. Rimke, G. Hehl, M. Beutler, P. Volz, A. Volkmer, and E. Büttner, "Tunable dual-wavelength two-picosecond light source for coherent raman scattering microscopy," in *Multiphoton Microscopy in the Biomedical Sciences XIV*, vol. 8948 (International Society for Optics and Photonics, 2014), p. 894816.
28. B. Lafuente, R. Downs, H. Yang, N. Stone, T. Armbruster, and R. Danisi, "Highlights in mineralogical crystallography," W. De Gruyter, Berlin pp. 1–30 (2015).
29. A. S. Mount, A. Wheeler, R. P. Paradkar, and D. Snider, "Hemocyte-mediated shell mineralization in the eastern oyster," Science **304**(5668), 297–300 (2004).
30. Y. Fu, H. Wang, R. Shi, and J.-X. Cheng, "Characterization of photodamage in coherent anti-stokes raman scattering microscopy," Opt. Express **14**(9), 3942 (2006).
31. H. Donner, L. Gao, and G. Mazza, "Separation and characterization of simple and malonylated anthocyanins in red onions, allium cepa l.," Food Res. Int. **30**(8), 637–643 (1997).
32. N. Gierlinger, T. Keplinger, and M. Harrington, "Imaging of plant cell walls by confocal raman microscopy," Nat. Protoc. **7**(9), 1694–1708 (2012).
33. I. Zeise, Z. Heiner, S. Holz, M. Joester, C. Büttner, and J. Kneipp, "Raman imaging of plant cell walls in sections of cucumis sativus," Plants **7**(1), 7 (2018).
34. J. De Gelder, K. De Gussem, P. Vandenabeele, and L. Moens, "Reference database of raman spectra of biological molecules," J. Raman Spectrosc. **38**(9), 1133–1147 (2007).
35. C. Brackmann, A. Bengtsson, M. L. Alminger, U. Svanberg, and A. Enejder, "Visualization of β-carotene and starch granules in plant cells using cars and shg microscopy," J. Raman Spectrosc. **42**(4), 586–592 (2011).
36. M. J. Moester, L. Zada, B. Fokker, F. Ariese, and J. F. de Boer, "Stimulated raman scattering microscopy with long wavelengths for improved imaging depth," J. Raman Spectrosc. **50**(9), 1321–1328 (2019).
37. E. R. Andresen, P. Berto, and H. Rigneault, "Stimulated raman scattering microscopy by spectral focusing and fiber-generated soliton as stokes pulse," Opt. Lett. **36**(13), 2387 (2011).